INORGANIC CHEMISTRY FRONTIERS

CCS 中国化学会 CHINESE CHEMICAL SOCIETY

ROYAL SOCIETY OF CHEMISTRY

Optical properties of undoped, Eu3+ doped and Li+ co-doped Y2Hf2O7 nanoparticles and polymer nanocomposite films

Journal:	*Inorganic Chemistry Frontiers*
Manuscript ID	QI-RES-09-2019-001181.R1
Article Type:	Research Article
Date Submitted by the Author:	28-Oct-2019
Complete List of Authors:	Gupta, Santosh; Bhabha Atomic Research Centre Zuniga, Jose; University of Texas Rio Grande Valley - Edinburg Campus Abdou, Maya; University of Texas Rio Grande Valley - Edinburg Campus Ghosh, P.S.; Bhabha Atomic Research Centre Mao, Yuanbing; Illinois Institute of Technology, Chemistry

Optical properties of undoped, Eu^{3+} doped and Li^{+} co-doped $Y_2Hf_2O_7$ nanoparticles and polymer nanocomposite films

Santosh K. Gupta[1,2], Jose P. Zuniga[1], Maya Abdou[1], P.S. Ghosh[3], and Yuanbing Mao[4*]

[1]Department of Chemistry, University of Texas Rio Grande Valley, 1201 West University Drive, Edinburg, Texas 78539, USA

[2]Radiochemistry Division, Bhabha Atomic Research Centre, Trombay, Mumbai-400085, India

[3]Materials Science Division, Bhabha Atomic Research Centre, Trombay, Mumbai-400085, India

[4]Department of Chemistry, Illinois Institute of Technology, 3105 South Dearborn Street, Chicago, IL 60616, USA

*To whom correspondence should be addressed. Electronic mail: ymao17@iit.edu, Tel.: +1-312-567-3815

Abstract

Desirable phosphors for lighting, scintillation and composite films must have good light absorption property, high concentration quenching, high quantum efficiency, and narrow color emission, etc. In this work, we first show that undoped yttrium hafnate $Y_2Hf_2O_7$ (YHO) nanoparticles (NPs) display dual blue and red bands after 330 nm light excitation. Based on density functional theory (DFT) calculations, these two emission bands are correlated with the defect states arising in the band-gap region of YHO due to the presence of neutral and charged oxygen defects. Once doped with Eu^{3+} ions, the YHO NPs show bright red emission, long excited state lifetime and stable color coordinates upon near-UV and X-ray excitations. Concentration quenching is active when Eu^{3+} doping reaches 10mol% with a critical distance of ~4.43 Å. This phenomenon indicates a high Eu^{3+} solubility within the YHO host and the absence of Eu^{3+} clusters. More importantly, the optical

performance of the YHOE NPs has been further improved by lithium co-doping. Origin of emission, structural stability, and the role of Li^+-co-doping are explored both experimentally and theoretically. DFT calculation results demonstrate that Li^+-co-doping increases the covalent character of Eu^{3+}-O^{-2} bonding in EuO_8 polyhedra. Furthermore, the YHOE NPs have been dispersed into polyvinyl alcohol (PVA) to make transparent nanocomposite films, which show strong red emission under excitations at 270 and 393 nm. Overall, we demonstrate that the YHO NPs with Eu^{3+} and (Eu^{3+}/Li^+) doping have high emission intensity and quantum efficiency under UV and X-ray excitations, which make them suitable as phosphors, scintillators and transparent films for lighting, imaging and detection applications.

Keywords: $Y_2Hf_2O_7$; Pyrochlore; Europium; Li^+; co-doping

1. Introduction

White LEDs are among the most demanded lighting source due to their high power output, long-term low cost, long lifespan and environment beingness.[1] The current white LEDs which use YAG:Ce yellow phosphor combined with blue emitting GaN semiconductor single crystal have issues related with its high color temperature and low color rendering index.[2-3] This is mainly due to the lack of desirable red phosphors which possess low CCT and improved color rendering index.[4-6]

Researchers exploring and studying optical materials are in continuous search for good candidates for X-ray scintillation, X-ray based luminescence deep-tissue imaging (DTI), and photodynamic therapy (PDT).[78-10] The advantage of using X-ray for DTI and PDT is that it allows deep tissue penetration, negligible X-ray scattering in tissue and negligible background for optical imaging

due to low auto fluorescence.[11] For all these applications, single crystals, bulk ceramic materials and glasses are mostly explored as efficient X-ray-phosphors.[7, 12-15] There are lots of issues with these materials, such as high cost and long-time of synthesis and process, lack of optical tunability and low scintillation efficiency.

In phosphor library, there are efficient blue ($BaMgAl_{10}O_{17}:Eu^{2+}$) and green ($SrSi_2O_2N_2:Eu^{2+}$, $Ba_2SiO_4:Eu^{2+}$) phosphors.[16-17] Finding efficient and inexpensive red phosphors is still difficult, especially those with good thermal stability, high concentration quenching, low defect density, etc. One of the major problems of achieving high emission efficiency from red phosphors designated for warm white LEDs and X-ray scintillators is their low quenching concentration of dopants.[18-19] Concentration quenching is a long withstanding problem that hinders the quest of highly efficient luminescent materials. Dexter and Schulman proposed that considerable fluorescence quenching takes place in bulk materials when activator or dopant concentration reaches 10^{-3}–10^{-2} M.[20] This problem poses serious hindrance on achieving high luminescence intensity for their applications.

Selection of compatible hosts plays a very important role in designing desirable red phosphors. Yttrium hafnate $Y_2Hf_2O_7$ (YHO) has been one of the most important pyrochlore materials for advanced technological applications such as enhancing structural and thermal properties of metals,[21] scintillators,[22] computer tomography (CT) and positron emission tomography (PET),[23] order-disorder phase transitions,[24] etc. YHO is also known to exhibit excellent thermal stability, radiation stability, ability to accommodate rare earth ions at both Y^{3+} and Hf^{4+} sites, etc. This makes $Y_2Hf_2O_7$ an excellent host for rare earth-based phosphors and scintillators.

Eu^{3+} ion has been chosen as dopant ion in this study for its narrow red emission, high color purity, symmetry sensitive red/orange emission, etc. Moreover, among various methods explored to enhance

the luminescence efficiency of bulk and powder phosphors,[25] Li^+ co-doping has been found to enhance their optical properties by modifying local crystal field around activator ions. With its small radius, Li^+ ions can be easily incorporated into the host lattice. However, to the best of our knowledge, there is no report on luminescence properties of undoped YHO, Eu^{3+}-doped YHO (YHOE), and Eu,Li co-doped YHO for photo/radioluminescent phosphors, especially no experiment reports on Li^+ doped YHO NPs and corresponding luminescence enhancement.[26-28] Therefore, in this work, we have synthesized YHO nanoparticles (NPs) and red light emitting YHOE NPs using a molten salt synthesis (MSS) method. We have also demonstrated that the former has dual blue and red emission bands and the latter has high concentration quenching of 10% and quantum efficiency of 12%. Intense radioluminescence from the YHOE NPs highlights their potential as X-ray scintillators. The co-doping with Li^+ ion has demonstrated with further improved emission output, quantum efficiency and excited state lifetime for the YHOE NPs.

To support our experimental results, we have performed density functional theory (DFT) based calculations to consider different charge states of oxygen vacancies (0, +1 and +2) by identifying their effects on the luminescence properties of YHO.[29-32] Moreover, oxygen defect formation energies are calculated to show the formation feasibility of these defects. The DFT studies confirmed the presence of neutral and ionized oxygen vacancies in the bandgap of the YHO NPs and the emission is correlated with these defect states. Furthermore, to explore the origin of emission, structural stability, and the role of Li^+-co-doping theoretically, we have use DFT calculation to demonstrate that Li^+-co-doping increases the covalent character of Eu^{3+}-O^{-2} bonding in EuO_8 polyhedra.

Polymer nanocomposites provide a potential solution to meet the technological requirements in virtue of the unique properties of NPs with the processability, structural flexibility, and thermal,

mechanical and optical properties of polymers and simultaneously prevent the agglomeration of NPs.[33-34] Incorporation of the YHOE NPs in a polymer system can significantly increase the physical parameter range beyond that of the host polymer and the NPs. In this work, we added the YHOE NPs into poly(vinyl alcohol (PVA) and made nanophosphor-polymer thin films (NPTF) which exhibit high transparency and uniform red emission.

2. Experimental

YHO, YHOE and Li-co-doped YHOE NPs were synthesized using a molten salt synthesis (MSS) method using KNO_3-$NaNO_3$ as the reaction medium at 650^oC.[35-38] The details of the synthesis method have been explained in electronic supplementary information (ESI) as S1. Moreover, the preparation of the NPTF employing the YHOE NPs and PVA has also been discussed in detail in S1.

The undoped sample is designated as YHO whereas the doped samples with Eu^{3+} concentrations of 0.5, 1.0, 2.0, 5.0, 7.5, 10.0, 12.5, and 15.0% as YHOE-0.5, YHOE-1.0, YHOE-2.0, YHOE-5.0, YHOE-7.5, YHOE-10.0, YHOE-12.5, and YHOE-15.0, respectively. Similarly, the Li^+ co-doped YHOE-0.5 NPs with Li^+ concentrations of 0.5, 1.0, 1.5, 2.0, 2.5 and 3.0% are designated as YHOE-0.5-Li0.5, YHOE-0.5-Li1.0, YHOE-0.5-Li1.5, YHOE-0.5-Li2.0, YHOE-0.5-Li2.5 and YHOE-0.5-Li3.0, respectively, and the 2.0% Li^+ co-doped YHOE NPs with Eu^{3+} concentrations of 0.5, 1.0, 2.0, 5.0, 7.5, 10.0, 12.5 and 15.0% are designated as YHOE-0.5-Li2.0, YHOE-1.0-Li2.0, YHOE-2.0-Li2.0, YHOE-5.0-Li2.0, YHOE-7.5-Li2.0, YHOE-10-Li2.0, YHOE-12.5-Li2.0 and YHOE-15.0-Li2.0 NPs, respectively.

The instrumental details of various characterization techniques such as X-ray diffraction (XRD), field emission scanning electron microscopy (FESEM), Raman spectroscopy, energy dispersive

spectroscopy (EDS), X-ray photoelectron spectroscopy (XPS), photoluminescence (PL), radioluminescence (RL) and time resolved emission spectroscopy (TRES) were described in ESI as S2. The theoretical methodology adopted in this work for density functional theory (DFT) is mentioned in ESI as S3. DFT calculated equilibrium volumes and bond-lengths using GGA/LDA (generalized gradient approximation/local density approximation) and bandgap using HSE06 (Heyd-Scuseria-Ernzerhof) method are provided in Table S1 (ESI#).

3. Results and discussion

3.1. Materials characterizations: XRD, Raman and SEM

Both XRD patterns (Figure S1a) and Raman spectra (Figure S1b) confirm the synthesized YHO and YHOE (0.5-15%) NPs have cubic fluorite structure. EDS and XPS spectra were recorded on one of the representative samples, i.e. YHOE-5, and the corresponding data were shown in Figure S1c and S1d, respectively. The calculated crystal size of these NPs (Table S2) is ~30 nm while the particle size estimated from the SEM images (Figure S2) ranges from 82 to 47 nm. Special quasi-random structure of YHO considered for the DFT simulations in disordered fluorite structure is shown in Figure S1e. The blue, black and red spheres represent Y, Hf and O atoms, respectively.

3.2. The YHO NPs

3.2.1 PL properties

The emission spectrum of the YHO NPs (Figure 1A) under 330 nm excitations displays two bands in the ranges of 400-500 nm and 680-730 nm corresponding to bluish-green and deep red emissions, respectively. We could not find much difference with 285 nm excitation except slight reduction in emission intensity of both the bands. Such multicolor emission is typical for the presence of defect states in the band gap of materials, specifically oxygen vacancies (OV), internal

defects and self-trapped excitons (STEs).[39] [40-41] [42] Oxygen vacancies can be neutral, singly ionized and doubly ionized. In the YHO NPs, there are possibly two kinds of structural defects contributing to the PL emissions. Their origins could be different based on the different excitation spectra observed under emission wavelengths of 445 nm and 710 nm (Figure S3a).[43-44] The color coordinate calculated for the YHO NPs confirms bluish-white emission (Figure S3bc).

3.2.2 DFT calculations

To probe the exact electronic transitions involved in such emissions from the YHO NPs, we employed DFT based HSE06 simulations to calculate electronic density of states (DOS) of ideal YHO and the change in electronic DOS in the presence of neutral (V^{0}_{O}), +1 (V^{+1}_{O}) and +2 (V^{+2}_{O}) charged oxygen vacancies. To generate defect structure, an oxygen atom was removed from an 88 atom SQS supercell. The generated defect structures were thoroughly optimized with respect to volume (or lattice parameter) and atomic positions (ESI S3, Table S1). Therefore, defect concentration in our calculation was 1/88 or 1.136%.

The total and orbital angular momentum resolved DOS of YHO with the Fermi level set to 0 eV (Figure 1B, i) shows that the electronic states below the Fermi level (or the valence band (VB)) are dominated by *p-d* bonding between O 2p and Hf 5d states. Conduction band (CB) is mainly composed of 4*d* states of Y and anti-bonding states of Hf 5*d* states. Our HSE06 calculated electronic bandgap of 3.98 eV demonstrates the insulating character of YHO. The total and angular momentum decomposed DOS due to the presence of neutral O vacancy (V^{0}_{O}) (Figure 1B, ii) demonstrates that the overall nature of the VB remains unaltered, but an impurity band appears 3.4 eV ahead of VB maximum in the bandgap and just below the Fermi level. This impurity state is doubly occupied and mainly contributed by La-d/f states and O-p states. The total and angular momentum decomposed DOS due to the presence of O vacancy with charge +1 (V_{O}^{+1}) (Figure 1B,

iii) presents that the V^{0}_{O} becomes V^{+1}_{O} by trapping a hole from its surrounding. The overall nature of the VB remains unaltered, but singly occupied impurity states appear 3.0 eV ahead of VB maxima. This impurity state is generated due to the spin-up component is filled with electrons as it is situated below the Fermi energy. The impurity levels are composed of Hf-*d* states and O-*p* states. The total and angular momentum decomposed DOS due to presence of O vacancy with charge +2 (V_{O}^{+2}) (Figure 1B, iv) shows that the overall nature of the VB remains unaltered, but an impurity band appears below CB minimum in the bandgap. The Fermi level is situated above the VB maximum. The impurity levels are composed of Hf-*d* states and O-*p* states in both the spin-up and spin-down components.

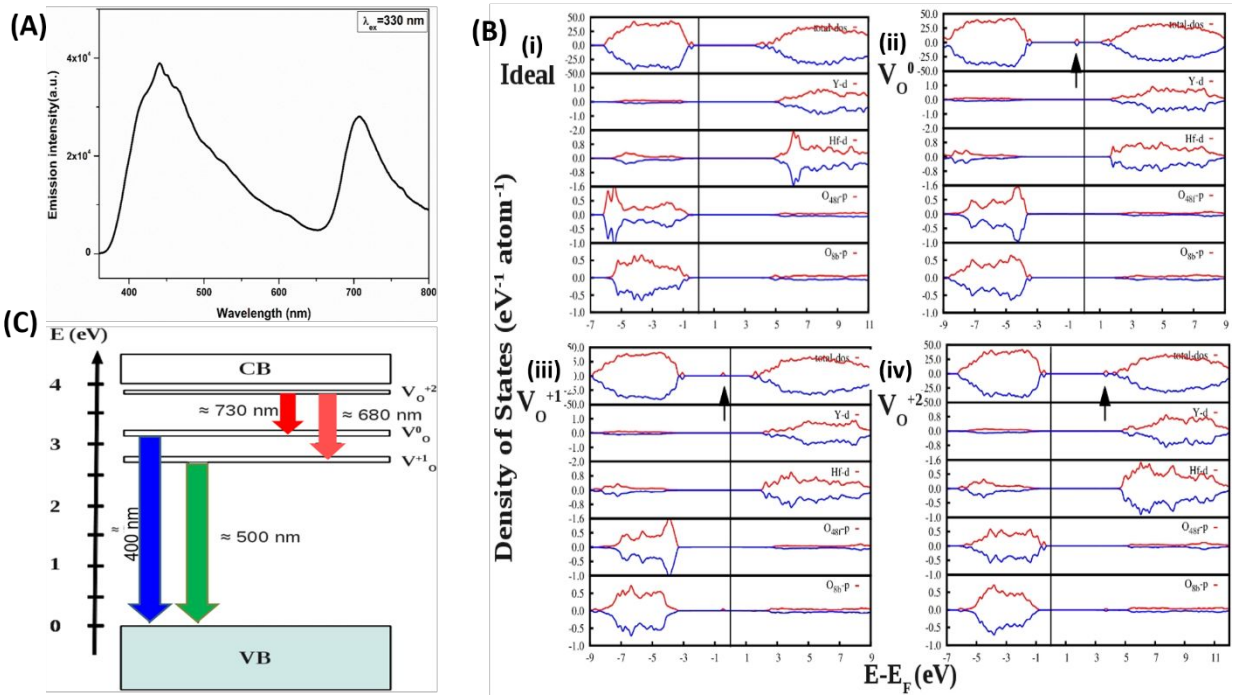

Figure 1. (A) Emission spectrum (λ_{ex} = 330 nm) of the YHO NPs, (B) HSE06 calculated total and angular momentum decomposed DOS of: (i) ideal defect free YHO and YHO with (ii) neutral oxygen vacancy (V^{0}_{O}), (iii) oxygen vacancy of charge +1 (V^{+1}_{O}), and (iv) oxygen vacancy of charge +2 (V^{+2}_{O}). Defect states are marked by an arrow in the bandgap. Vertical lines at 0 eV present Fermi energy. (C) A summary of defect state distribution within the band gap of YHO.

Based on our DFT-HSE06 calculations, we have summarized the location of defect states in the band-gap region of YHO (Figure 1C). The broad emission peak around 400-500 nm from the YHO NPs corresponds to an optical emission between states situated 3.0-2.5 eV from each other, i.e. the optical emission between defect states of V^0_O and V^{+1}_O to VB (marked by the blue and green arrows). In YHO, defect states near 4.0 eV are consist of V_O^{+2}. The broad emission peak around 680-730 nm region which is situated 1.7-1.8 eV away from each other originates from the transition between V_O^{+2} defect state → (V^0_O, V^{+1}_O) (marked by the red and deep red arrows). Therefore, our DFT-HSE06 results qualitatively provide an explanation for the origins of the broad emission peaks from the YHO NPs.

The DFT-GGA calculated oxygen defect formation energies in the dilute limit for neutral (V_O^0) and charged (V_O^{1+} and V_O^{2+}) oxygen defects (Figure S3c) indicate that the formation of V_O^{2+} defects is most favored near the VB compared to those of V_O^{1+} and neutral oxygen defects and that the oxygen vacancies have a tendency to donate electrons.[45] The formation of a neutral oxygen vacancy is energetically less favorable compared to that of charged oxygen defects. The vacancy formation energies of 1+ and 2+ oxygen defects become close with a difference of 0.5 eV at Fermi level. With increasing Fermi energy, the vacancy formation energy of V_O^{+1} defect becomes most favorable compared to those of V_O^0 and V_O^{+2} defects. As the vacancy formation energies of V_O^0, V_O^{1+} and V_O^{2+}defects get close, oxygen defects are expected to strongly participate in the PL emission from the YHO NPs.

3.3. The YHOE NPs

3.3.1 Excitation PL spectra

In the PL excitation spectra (Figure 2a), the broad band in the range of 240–310 nm can be attributed to $O^{2-}\rightarrow Eu^{3+}$ charge transfer (CT) transition corresponding to electron transfer from filled 2p shell of O^{2-} ions to empty 4f shell of Eu^{3+} ions. There is no regular trend of the energy of the CT band or its FWHM as a function of Eu^{3+}concentration. The sharp peaks in the range of 350-550 nm are related to interconfigurational $(Xe)4f^6\rightarrow(Xe)4f^6$ transitions of Eu^{3+} ions. The most attractive features of the excitation spectra are the highly intense near UV (393 nm) and blue (465 nm) bands due to $^7F_0\rightarrow{}^5L_6$ and $^7F_0\rightarrow{}^5D_2$ transitions, which indicate that the YHOE NPs can serve as color converters for LED applications because of their high spectral overlap cross section with emission spectra of efficient LEDs.

3.3.2 Emission PL spectra

The YHOE NPs show bright red luminescence when excited with UV lamp (Figure 2b) with characteristic Eu^{3+} spectral features of $^5D_0\rightarrow{}^7F_J$ transitions (J = 1-4). Specifically, the emission peaks at 592, 612, 653, and 710 nm are from $^5D_0\rightarrow{}^7F_1$, $^5D_0\rightarrow{}^7F_2$, $^5D_0\rightarrow{}^7F_3$ and $^5D_0\rightarrow{}^7F_4$ transitions, respectively. Among them, the 592 nm peak is the magnetic dipole $^5D_0\rightarrow{}^7F_1$ transition (MDT) which is independent of chemical environment surrounding Eu^{3+} ions. The most intense band at 612 nm is ascribed to hypersensitive electric dipole $^5D_0\rightarrow{}^7F_2$ transition (EDT), which is normally observed when Eu^{3+} ions are localized at sites without center of inversion (C_i). The YHOE NPs have highly disordered fluorite structure as confirmed by XRD and Raman spectroscopy (Figure S1). Therefore, most Eu^{3+} ions are localized in highly disordered fluorite structure which lacks inversion symmetry. Consequently, highly intense red emissions from the EDTs of $^5D_0\rightarrow{}^7F_2$ and $^5D_0\rightarrow{}^7F_4$ are observed and the intensity of EDT peak is higher than that of MDT peak. Based on these concentration dependent emission profiles, the dominance of the EDT over MDT at all Eu^{3+} doping concentration indicates the majority of Eu^{3+} ions have asymmetric

local surrounding. Figure S4 (a), (b) and (c) shows the HSE06 calculated DOS of Eu^{3+} doped YHO (in Y^{3+} site) in a system containing V^{0}_{O}, V^{+1}_{O} and V^{+2}_{O}, respectively. The overall DOS is similar to their V^{0}_{O}, V^{+1}_{O} and V^{+2}_{O} counterpart. The Eu^{3+} doping at Y^{3+} site lifts the degeneracy in the defect states and generates shallow defect states near to CB minima. The Eu-*d* states are present throughout the VB and CB energy region of YHO and good matching in distribution of Eu-*d* states can be found with the VB/CB energy region of YHO. This allows for good energy transfer efficiency from host to Eu^{3+} ion.

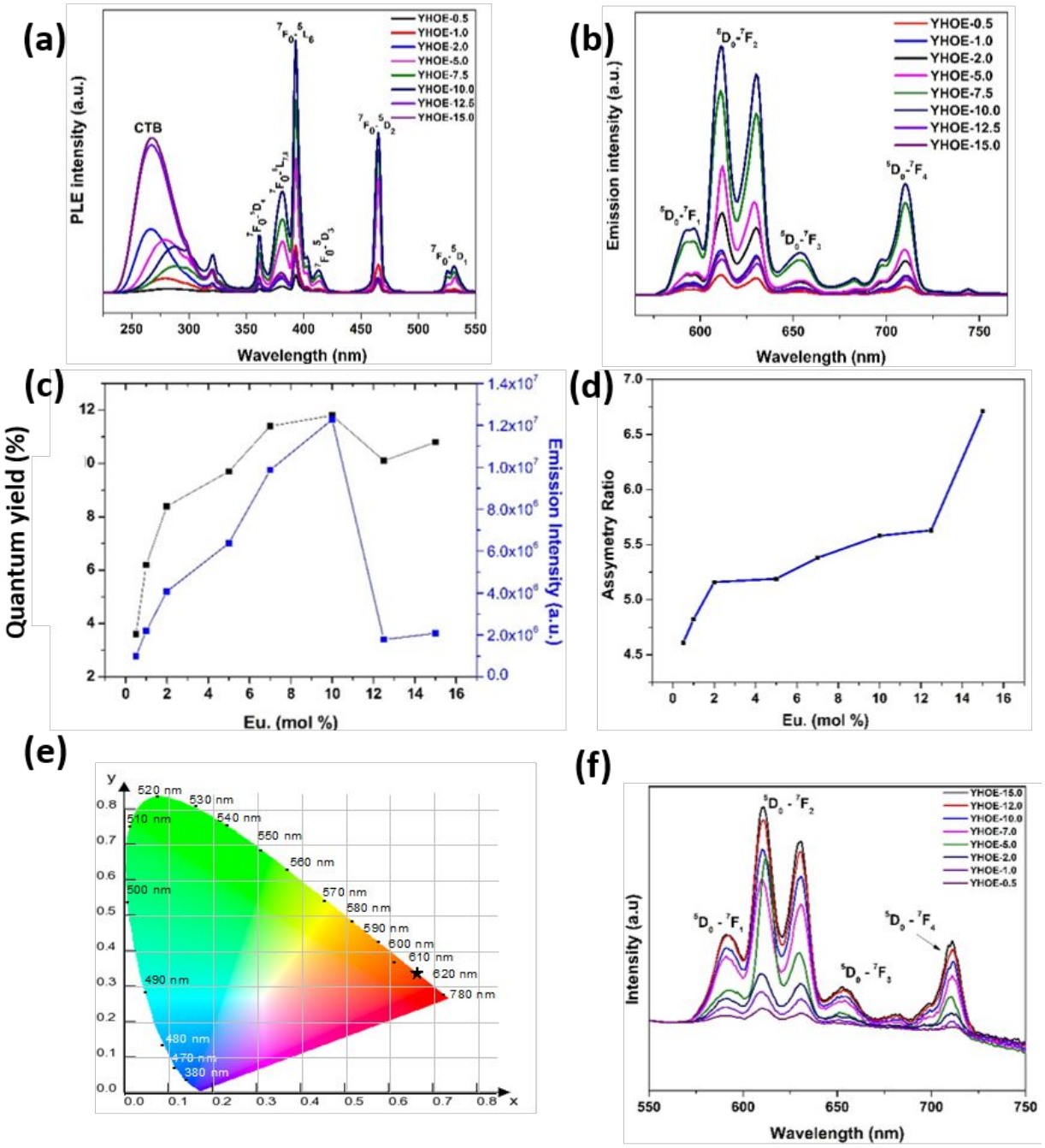

Figure 2. (a) PL excitation spectra (λ_{em} = 612 nm), (b) PL emission spectra (λ_{ex} = 393 nm), (c) quantum yield and integrated PL emission intensity of the $^5D_0 \rightarrow {}^7F_2$ transition (λ_{ex} = 393 nm) as a function of Eu^{3+} doping concentration, (d) asymmetry ratio, (e) chromaticity diagram (of the YHOE-10.0 NPs), and (f) RL spectra of the YHOE NPs.

PL emission intensity of the YHOE NPs is strongly governed by the dopant concentration (Figure 2c). The integral emission intensity (φ) from 600 to 640 nm corresponding to the $^5D_0 \rightarrow {}^7F_2$ transition progressively increases as Eu^{3+} doping concentration increases from 0.5 to 10.0mol% (Figure 2c). For Eu^{3+} doping concentrations higher than 10.0%, the corresponding φ decreases, which is attributed to the concentration quenching phenomenon. Therefore, the critical quenching concentration of our YHOE NPs is 10.0%, which is high enough to produce efficient nanophosphors.

For dopant-based phosphors, the critical quenching concentration strongly depends on the solubility of dopant ions in host matrix which depends on the selections of dopant and host. In most phosphors, low solid solubility of dopant ions leads to their segregation in host lattice, which results in concentration quenching at low doping concentration. As listed in Table S3, when the trivalent Eu^{3+} dopant occupies divalent and/or tetravalent sites, charge compensating defects lead to high strain which limits quenching concentration to low values. Concentration quenching happens when excitation energy (E_{exc}) migrates and reaches quenching center, where E_{exc} is lost nonradiatively rather than being converted into radiative emission of photon. High concentration quenching relies on the intrinsic crystal structure of hosts and by large nanocrystals can accommodate more active doping ions compared to bulk materials. Moreover, high concentration quenching of the YHOE NPs indicates trivalent europium ions with red emission. For our YHOE NPs, Eu^{3+} and Y^{3+} ions have the same ionic charge and similar ionic size, which results in high solid solubility and uniform dispersion of Eu^{3+} ions in the YHO matrix even at high doping concentration. Nanocrystalline nature of the synthesized YHOE NPs also aids to achieve high quenching concentration. Improvement in quenching concentrations were also observed in going from bulk to nano in other RE doped nanophosphor as well.[46-47] This is attributed to low density

of traps in nanosystems due to limited primitive cell per particle.[47]Also doping uniformity in nanomaterials minimizes segregation of ions and prevent local concentration quenching.[48]

One can calculate the minimum distance between dopant ions and quenching centers that facilitate non-radiative energy transfer and leads to decrease of emission intensity using an empirical relation given by Blasse:[49]

$$r_c = 2\left(\frac{3V}{4\pi X_c N}\right)^{\frac{1}{3}} \quad (1)$$

where r_c is the critical distance between dopant ion and quenching center, V is the volume of the unit cell of host matrix, X_c is the critical concentration of dopant ions after which concentration quenching takes place, and N is the number of cations per unit cell of host lattice. For YHO host lattice, $V = 145.83$ Å^3, $N = 32$ (four formula units per unit cell), and $X_c = 0.1$, so the calculated critical distance is 4.43 Å. In other words, the Eu^{3+}-Eu^{3+} distance in the YHOE NPs is smaller than 10 Å. Therefore, for the concentration quenching of our YHOE NPs, exchange interaction is the main mode of non-radiative energy transfer among the Eu^{3+} ions in the YHO host.

3.3.3 Asymmetry ratio

The integral intensity ratio of the EDT ($^5D_0 \rightarrow {}^7F_2$) and MDT ($^5D_0 \rightarrow {}^7F_1$) peaks, known as asymmetry ratio (R_{21}), defines the structural distortion around Eu^{3+} ions in host lattice. The R_{21} of the YHOE NPs increases with increasing Eu^{3+} dopant concentration progressively (Figure 4d). This trend suggests a more favorable asymmetric environment of Eu^{3+} ion in the YHO lattice with increasing doping level, which indicates a more disordered YHO matrix lattice at higher doping concentration. Therefore, the electric dipole induced emission ($^5D_o - {}^7F_2$) is the most intense peak from the YHOE NPs under near UV excitation. Correspondingly, the asymmetry ratio of the YHOE-15.0 NPs is the highest, which is close to 7. Based on Table S4, the YHOE NPs display the highest asymmetry ratio compared to reported Eu^{3+} doped pyrochlore phosphors, which

suggests that they have high red color purity for achieving desirable performance in phosphor driven white LEDs.

3.3.4 Quantum yield

As an important parameter for commercial and practical purposes, the quantum yield (QY) of the YHOE NPs were measured and calculated using the following equation:[50]

$$QY = \frac{\int F_S}{\int L_R + \int L_S} \quad (2)$$

where F_S represents the emission spectrum of a sample, L_R is the spectrum of the excitation light from empty integrated sphere (without sample), and L_S means the excitation spectrum of the excited sample. The experiments were done similar to our previous publications.[51] The QY value of the YHOE NPs increases from 3.5% to 12% as the Eu^{3+} doping concentration increases from 0.5% to 10.0% and then slight reduces (Figure 4e). The latter is again attributed to non-radiative energy transfer among Eu^{3+} ions at high doping concentration causing concentration quenching. Among several reported Eu^{3+} doped pyrochlore phosphors, the QY of the YHOE NPs is decent (Table S5).

3.3.5 Colorimetric performance

Since there is no obvious spectral profile change of the YHOE NPs as a function of Eu^{3+} doping concentration, Commission Internationaledel' Eclairage (CIE) chromaticity coordinates were evaluated for the YHOE-10.0 NPs. The corresponding CIE index diagram shows that the YHOE NPs emit intense red light with CIE coordinates of 0.665 and 0.343 (Figure 2e), which are in close agreement with the international standard chromaticity coordinates of the commercial red phosphors: $Y_2O_2S:Eu^{3+}$ (x = 0.642 and y = 0.341) and $Y_2O_3:Eu^{3+}$ (x = 0.650 and y = 0.356).[5230, 35-36, 44]

3.3.6 Lifetime spectra

All the YHOE NPs exhibit biexponential decay under 393 nm excitation and 612 nm emission wavelengths (Figure S5a) and can be fitted using the equation:

$$I(t)= A_1 \exp(-t/\tau_1) + A_2 \exp(-t/\tau_2) \quad (3)$$

where $I(t)$ is the PL emission intensity at time t, A_1& A_2 are residual weighting factor of each lifetime, t is time of measurements, τ_1 and τ_2 are the lifetime values of the first and the second components, respectively. Biexponential PL decay behavior can be caused by different energy transfer and nonradiative decay of dopant ions localized near the surface and core of NPs and non-uniform distribution of dopant ions in host matrix.[53] For our defect fluorite structured YHOE NPs, there are two cation polyhedral: an ideal cube-like YO_8 and a highly distorted HfO_6. Usually the long lifetime component ($\tau_{2)}$ is attributed to lanthanide dopants located at symmetric environment as f-f transitions are forbidden by La-Porte selection rule.[54-55] On the other hand, the short lifetime component ($\tau_{1)}$ is assigned to lanthanide dopants localized at asymmetric environment. In our case, the $\tau_2$component (2.0-2.6 ms) is attributed to Eu^{3+} ions occupying the highly symmetric YO_8cubedue to the closeness of ionic radii and matching trivalent charge of Eu^{3+} and Y^{3+}. The τ_1 component (0.56-1.05 ms) is attributed to Eu^{3+} ions occupying the distorted HfO_6 octahedra.

The average lifetime value of the YHOE NPs increases from 1.78 to 2.02ms with increasing Eu^{3+}doping concentration from 0.5% to 10% and then decreases with further increase of Eu^{3+} (Table S6 and Figure S5b), similar to the observed trends of their PL intensity and QY (Figures2c). Moreover, the fraction of the long-lived species situated at Y^{3+} site is much higher than the short-lived species localised at Hf^{4+} site (Table S3).[30, 35-36, 38, 44, 56-57] The lifetime values of our YHOE NPs are similar to those reported for other Eu^{3+} doped pyrochlore phosphors (Table S7).

3.3.7. Structural stability of Eu^{3+} dopant ions in the YHO host

To understand the structural stability of Eu^{3+} dopant ions in the YHO host, the cohesive energies of

Eu^{3+}-doped YHO were calculated for Eu^{3+} doping at Y^{3+} site and Hf^{4+} sites separately using DFT based calculations. Such DFT based calculations have been used to predict the structural stability of dopant ions in other $A_2M_2O_7$ compositions, particularly for hafnate and zirconate based systems.[30, 35-36, 44] This is done by calculating cohesive energy of Eu^{3+} at A^{3+} and M^{4+} sites. The one with minimum cohesive energy has higher structural stability and vice versa.[30, 35, 44] In our DFT calculations, a doping level of Eu^{3+} ions of 1/88 (1.136%) in YHO was considered and full structural relaxations were performed. The Eu-O bond distances when Eu^{3+} doped at Y^{3+}/ Hf^{4+} sites are mention in Table 1. From this table it is clearly seen that the distribution of Eu-O bond lengths is smaller when Eu^{+3} is doped at Y^{3+} site compared to Hf^{4+} site, which signifies that Eu^{3+} substitution is favorable at Y^{3+} site considering their same charge state and closeness in ionic sizes. Therefore, from these DFT calculations we can conclude that Y^{3+} site is energetically more favorable compared to the Hf^{4+} site implying preferential occupation of Eu^{3+} ions at Y^{3+} site.

Moreover, our DFT calculated results are in corroboration with experimentally measured lifetime values, which show that the fraction of the long-lived species occupying the Y^{3+} site is much more than that of the short-lived species occupying the Hf^{4+} site.

Table 1. DFT calculated Eu-O bond distances when Eu^{3+} is doped at Y^{3+}/Hf^{4+} site in YHOE NPs.

	Eu-O bond distances							
Eu doped at Hf^{4+} site	2.29	2.29	2.41	2.41	2.43	2.44	2.60	2.72
Eu doped at Y^{3+} site	2.30	2.35	2.35	2.40	2.44	2.50	2.51	2.56

3.3.7 RL

When ionizing radiation is absorbed by a sample, electron–hole pairs are created following a typical scintillation mechanism. The emitted light is intense if the band gap between the excited state and the highest component of the ground state multiplet is large. RL light is generated when host absorbs X-ray photons and electrons are promoted to the excitation level $^5D_0$ of Eu^{3+}wherein they get activated. This is followed by the recombination of activated electrons and holes, which finally transfer and recombine energy to emitting centers (Eu^{3+} ions in this case). The room temperature RL emission spectra of the YHOE NPs (Figure 2f) show similar profiles as their PL spectra. Both types of spectra exhibit bands centered at 592 nm ($^5D_0 \rightarrow {}^7F_1$), 613 nm ($^5D_0 \rightarrow {}^7F_2$), 653 nm ($^5D_0 \rightarrow {}^7F_3$) and 702 nm ($^5D_0 \rightarrow {}^7F_4$) of Eu^{3+} ions. Moreover, the intensity of the hypersensitive EDT peak is much higher than that of the MDT peak under X-ray excitation too, which indicate that the majority of Eu^{3+} ions is localized at a highly asymmetric environment lacking centre of symmetry. This confirms that X-ray irradiation can generate similar emission spectra as UV light. However, the RL emission intensity is lower than the PL emission intensity which could be due to the lower power density of the applied X-ray under normal conditions than that of the UV excitation source (5 mW/cm^2). Unlike the observed PL concentration quenching at 10% Eu^{3+} doping level, in case of PL, no RL quenching was observed from our YHOE NPs with the highest Eu^{3+} doping level of 15% in this study. For efficient scintillators, heavy elements compositing host materials are crucial for photoelectric absorption of X-rays. With the heavy element constituent of Hf (Z = 72) and the intrinsic defect emission, YHO serves as an efficient X-ray antenna by absorbing X-ray photons and transferring them to Eu^{3+} activators. Thus, our YHOE NPs exhibit high efficiency of X-ray excited luminescence compared to other scintillators without heavy atomic component. The mechanism of X-ray excited luminescence in YHOE NPs is explained in ESI file S7 along with schematic shown in Figure S6.

3.4. Li Co-Doped YHOE NPs

3.4.1 Luminescence spectroscopy studies

To study the co-doping effect of Li^+ on the luminescence performance of the YHOE NPs, we first kept the Eu^{3+} concentration at 0.5% and varied the Li^+ concentration between 0 and 3.0%.From the PL emission spectra of the Li^+ co-doped YHOE-0.5 NPs (Figure 3a), the optimal co-doping concentration of Li^+ with maximum PL emission output is 2.0% mainly due to enhanced radiative transition rate on Li^+ co-doping.[58] The excitation spectra from the same series of samples also show similar trends (Figure S7a). There are several factors responsible for PL enhancement of Li^+ co-doping of phosphors, including modification of symmetry of primary dopant ions, reduced defect, charge compensation and induction of oxygen vacancies into host crystals.[59] After optimum Li^+ co-doping concentration of 2.0%, the created oxygen vacancies and other defects cause suppression of PL emission output by providing non-radiative pathways.[60]

With the optimum Li+ co-doping concentration of 2.0%, now the quenching concentration was found to be 12.5% of Eu^{3+} ions in the YHO host NPs (Figure 3b), a 2.5% increase from the YHOE NPs without Li^+ co-doping (Figure 2c). It is believed that this increase is endowed by a better control over the defects by means of Li^+ co-doping.[61]Similarly, the PL excitation spectra of the Li^+ co-doped YHOE NPs show similar trends (Figure S7b).

Figure 3c compares the PL excitation spectra of the YHOE-12.5 NPs before and after 2.0% Li^+ co-doping. There are some interesting features observed after Li^+ co-doping. First, the CTB energy becomes lower after co-doping whereas the reverse is true for the f-f transitions at 395 and 465 nm. The former can be attributed to a reduction in ionic character of the YHO host in the presence of highly electropositive Li^+ ion. There may be also chances that the Li^+ co-doping enhances the covalency of the Eu^{3+}-O^{2-} bond and the coordination environment of the Eu^{3+} ion site to reduce

the charge transfer energy.[52] Overall, Li^+ co-doping improves the absorption of the YHOE NPs in the region of 350-550 nm which is important for their commercial applications from the perspective of near UV and blue light excitations.

From the PL emission spectra of the YHOE-12.5 NPs before and after 2.0% Li^+ co-doping, we can see that the emission intensity doubles (Figure3d). Similar enhancement of PL emission has been reported from a few Eu^{3+} doped phosphors in the literature although quantification on the extent of enhancement is lacking.[58-60] There is an enhancement in decay lifetime of the YHOE NPs from 2.02 ms to 2.43 ms upon Li^+ co-doping (Figure 3e). Li^+ co-doping has also been explored to enhance emission output of lanthanide doped phosphors using non-optical excitation processes such as cathodoluminescence or X-ray excitation.[62] Upon Li^+ co-doping, RL intensity of the YHOE-12.5 NPs has been enhanced (Figure 3f). Similar RL intensity enhancement was also obtained from Y_2O_3:Eu NPs upon Li^+ co-doping.[63] These observations are correlated with the decrease of the asymmetry ratio R_{21} (from 4.62 to 3.85) and increase of QY (from 12 to 13.6 %) (Figure 3g). Small ions like Li^+ can readily enter the interstitial sites of the YHO host to lower its crystal field symmetry around Eu^{3+} ions. Lattice altercation is induced by the formation of Eu....O....Li types of moiety wherein the local surrounding of the Eu^{3+} ions gets modified due to redistribution of electron density around oxygen ions, therefore more electrons are pulled toward Eu^{3+} ions.[64] Moreover, incorporation of Li^+ ions at Y^{3+} site leads to the generation of oxygen vacancies through the following reaction:

$$Li^{\cdot} + 2Y_Y^{\cdot\cdot\cdot} \leftrightarrow 2Li_Y'' + O_O^x + V_O^{\cdot\cdot} \quad (4)$$

The $V_O^{\cdot\cdot}$ defects act as the sensitizer for Eu^{3+} ions and cause very efficient radiative energy transfer to Eu^{3+} ions due to strong mixing of CTB, thus leads to increase of emission intensity.[65] After Li^+ co-doping, lower R_{21} of the YHOE-12.5 NPs indicates more symmetric environment around Eu^{3+}

ions for longer decay lifetime. This aspect is highly useful in exploring NPs for fluoroimmunoassays. Moreover, Li^+ incorporation improves crystallinity of phosphor host,[62] reduces surface defects, enhances phonon-electron interaction, reduces internal reflections and decreases non-radiative transitions,[66-67] thus improvement of emission intensity.[68-69]

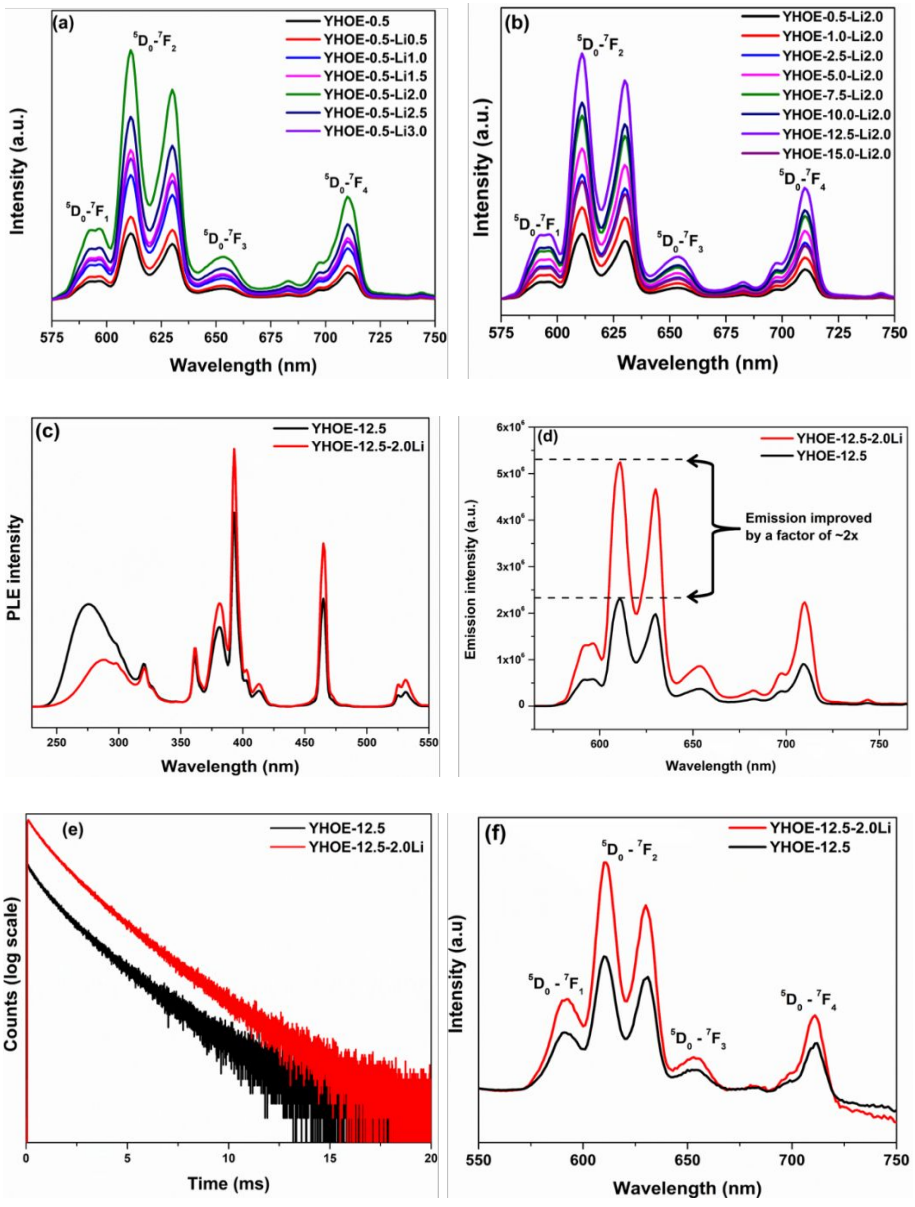

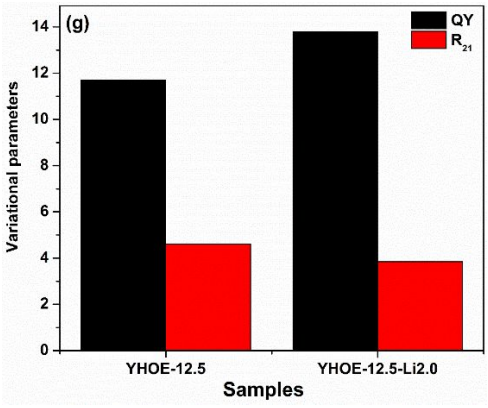

Figure 3. (a) PL emission spectra of the YHOE-0.5 NPs with different Li^+ co-doping concentrations. (b) PL emission spectra of the YHOE NPs with 2.0% Li^+ co-doping concentration but with various Eu^{3+} concentrations. Comparison of the YHOE-12.5 NPs before and after 2.0% Li^+ co-doping: (c) excitation spectra, (d) emission spectra, (e) luminescence decay profiles, (f) RL spectra, and (g) QY and asymmetry ratio.

3.4.2 DFT studies on the role of Li^+ co-doping

To further understand the effects of Li co-doping on the YHOE NPs, two separate DFT calculations were performed. In one calculation, single Eu^{3+} ion substituted an Y^{3+} site of 88-atom SQS cell to form EuO_8 polyhedra. On another calculation, single Li atom was substituted in EuO_8 polyhedra in place of an oxygen atom. These two 88 atom SQS cell was optimized with respect to volume and atomic positions. Figures4a and 4c clearly show that electron clouds are distributed around O atoms non-spherically indicating Eu^{3+}-O^{2-} bonding consists of ionic and covalent character. Upon Li^+ co-doping, an additional electron cloud appears in the Li^+ co-doped EuO_8 polyhedra marked by the black arrow (Figures 4b and 4d). As a result, after Li^+ co-doping, an almost spherical charge distribution around Eu^{3+} ion suffers distortion and becomes elongated which implies increase in the covalent character of Eu^{3+}-O^{-2} bonding (Figure 4c *vs* Figure 4d). This phenomenon agrees with our PL excitation spectral data

which suggested a reduction of the CTB energy upon Li^{+} co-doping due to the increasing covalent character of Eu^{3+}-O^{-2} bond. Figure S8 shows the HSE06 calculated DOS of Eu^{3+} doped and Li co-doped YHO (in Y^{3+} site) in a system containing V^{0}_{O}, V^{+1}_{O} and V^{+2}_{O}, respectively. Li co-doping generates shallow defect states near CB minima and Li-*p* states are contributing at the defect states in all oxygen vacancy type. Therefore, it is expected that Li co-doping with Eu^{3+} doping will influence the defect related emission in YHO and may improves the emission intensity and quantum efficiency.

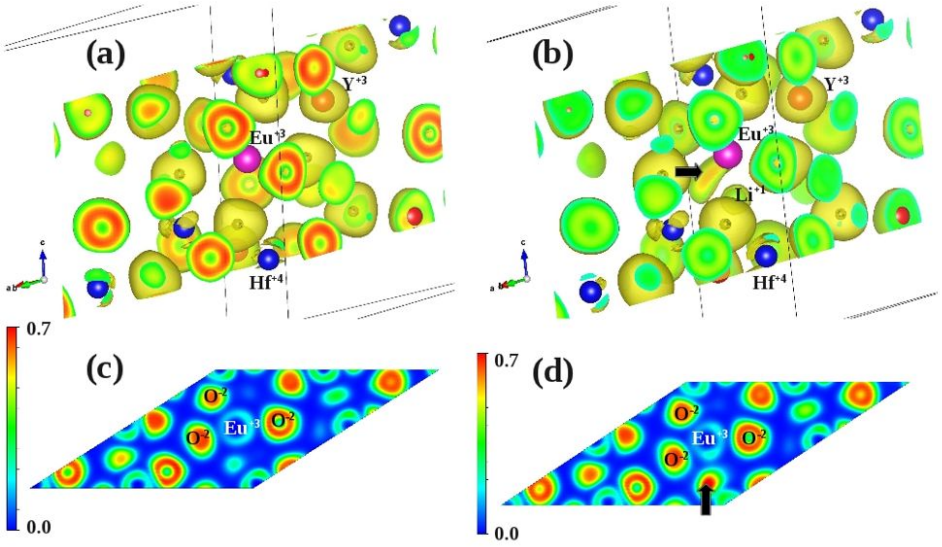

Figure 4. Electron Localization function (ELF) plots of (a) Eu^{3+} substituted in YO_8 polyhedra and (b) Li co-doped (in O^{2-} site) and Eu^{3+} substituted in YO_8 polyhedra (Eu in pink, Y in red, Hf in blue, O in black, and Li atom in green). The 2-dimensional charge density distribution (in e/Å^3) plots in (002) plane for (c) Eu^{3+} substituted and (d) Li co-doped and Eu^{3+} substituted cases.

3.5 Nanophosphor-polymer thin films

The excitation spectrum of the NPTF under 612 nm emission (Figure 5a) displayed similar features to that of the YHOE NPs. There is a broadband peak around 259 nm corresponding to

$O^{2-} \rightarrow Eu^{3+}$ CT along the f-f bands in the range of 350-550 nm similar to those of the YHOE NPs. On the other hand, emission spectra (Figure 5b) show typical Eu^{3+} profile under 259 nm and 393 nm excitations. The peak positions of $^5D_0 \rightarrow {}^7F_2$ and $^5D_0 \rightarrow {}^7F_1$ transitions are unaltered after the YHOE NPs dispersed in PVA matrix. The relative excitation and emission intensities of the NPTF are lower than those of the YHOE NPs because of the presence of lower number of Eu^{3+} ions per unit volume. In addition, the NPTF is highly transparent (Figure 5c) for various potential applications in the development of optoelectronic devices. Uniform red emission is also observed from the NPTF (Figure 5d) to confirm the homogeneous distribution of the YHOE NPs in PVA matrix. The luminescence decay profile (Figure 5e) displays monoexponential behavior with a lifetime value of 1.73 ms. This is different from the YHOE NPs themselves which displayed biexponential decay. This can be ascribed to more homogenous environment offered by dispersing the YHOE NPs in the polymeric PVA matrix.

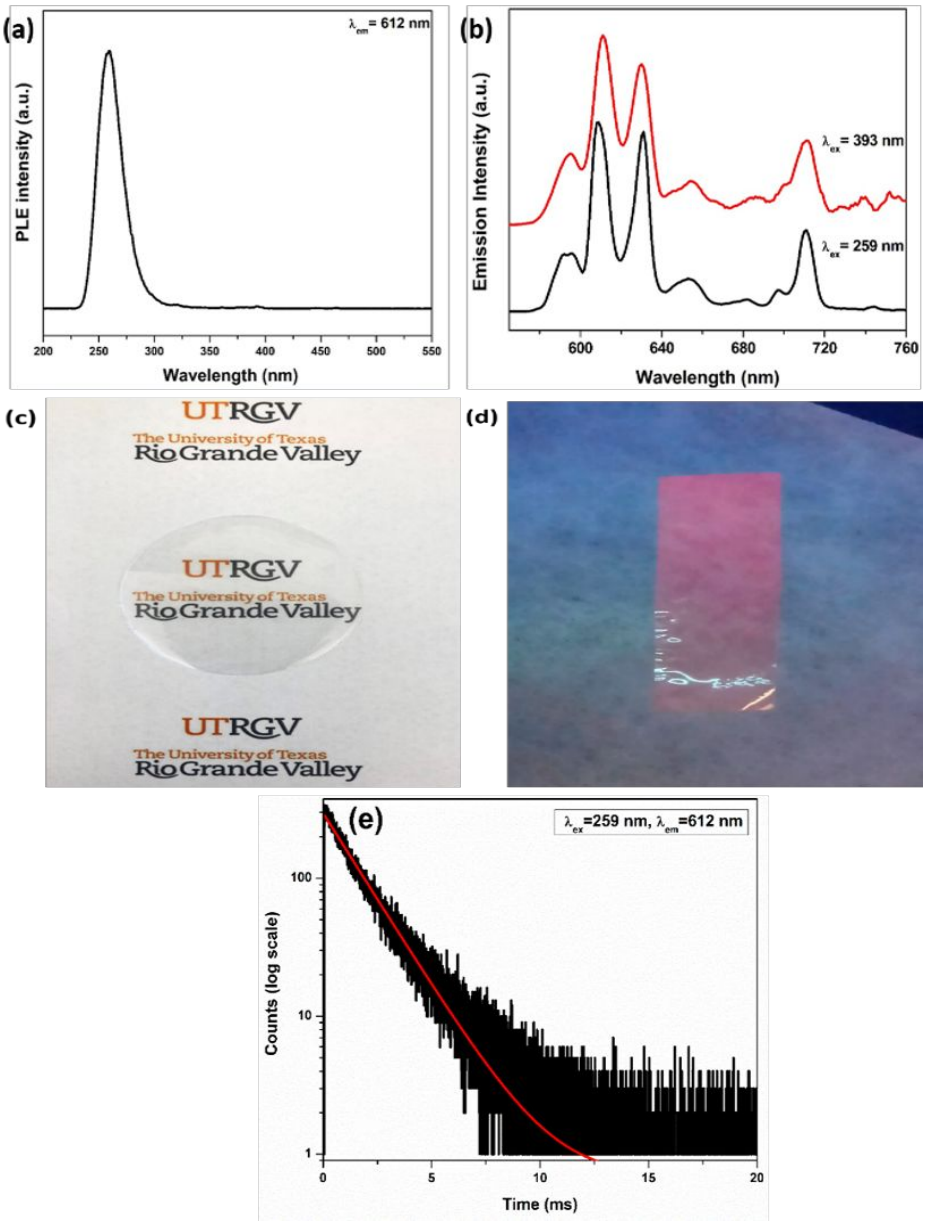

Figure 5. The YHOE NPs-containing NPTFs: (a) excitation spectrum, (b) emission spectra (λ_{ex} = 259 nm and 393 nm), (c) photograph, (d) corresponding red emission under near UV excitation, and (e) luminescence decay profile.

Conclusion

In this work, YHO, YHOE (Eu^{3+} = 0.5-15%) and Li^{+}-codoped YHOE NPs were synthesized at 650^{o}C using molten salt synthesis. The undoped YHO NPs displayed violet and blue emissions under 330 nm excitation, which have been attributed of the presence of ionized oxygen vacancies in its bandgap based on DFT calculations. Eu^{3+} doping leads to intense red emission at 612 nm, long luminescence decay time and high concentration quenching. Since Eu^{3+} and Y^{3+} have the same ionic charge and similar ionic size, Eu^{3+} ions exhibit high solubility in the YHO host. Higher affinity of Eu^{3+} for Y^{3+} is also justified using DFT calculated cohesive energy at both Y^{3+} and Hf^{4+} site. This results in uniform dispersion of Eu^{3+} ions in the YHO matrix even at high doping concentration. Co-doping Li^{+} ions in the YHOE lattice enhances the quantum efficiency and excited state lifetime of the YHOE NPs. The DFT results show Li^{+} co-doping increases the covalent character of Eu^{3+}-O^{-2} bonding in EuO_8 polyhedra. Our Li^{+}-codoped YHOE NPs display optimum photo- and radioluminescence output which highlight their application potentials in solid state lighting and X-ray phosphors. In summary, our work demonstrated a highly efficient material for optoelectronics and scintillator applications with high concentration quenching, high color purity and long lifetime. The YHOE NPs is also explored for making nanophosphor-polymer thin films which exhibited good emission property, high transparency and uniform red emission. They are expected for potential applications in life science and optoelectronics.

Acknowledgement

YM thanks the financial support by the National Science Foundation under CHE (award #1710160) and the IIT startup funds. SKG thanks the United States-India Education Foundation (USIEF) and the Institute of International Education (IIE) for his Fulbright Nehru Postdoctoral

Fellowship (Award# 2268/FNPDR/2017). We also thank Dr. J. Liu for technical support on the preparation of the YHOE-PVA nanocomposite thin films.

Supporting Information Available:

Experimental part consisting of synthesis, instrumentation and theoretical methodology, DFT calculate bond length, cell volume and band gap, XRD patterns, lattice parameter and crystallite size, Raman, SEM, PL decay curves (λ_{ex} = 393 nm and λ_{em} = 612 nm) , plots of decay lifetime as a function of Eu^{3+} concentration of the YHOE NPs, lifetime values of the YHOE NPs, PL excitation spectra of the YHOE-0.5 NPs at different Li^{+} cooping concentrations, and PL excitation spectra of the YHOE NPs at different Eu^{3+}concentrations with the same Li^{+} concentration of 2.0% for the YHOE NPs.

The authors declare no competing financial interest.

References:

1. Jiang, C.; Peng, M.; Srivastava, A. M.; Li, L.; G. Brik, M., Mn^{4+}-Doped Heterodialkaline Fluorogermanate Red Phosphor with High Quantum Yield and Spectral Luminous Efficacy for Warm-White-Light-Emitting Device Application. *Inorganic Chemistry* **2018,***57*, 14705-14714.
2. Zhang, Z.; Ma, C.; Gautier, R.; Molokeev, M. S.; Liu, Q.; Xia, Z., Structural Confinement toward Giant Enhancement of Red Emission in Mn^{2+}-Based Phosphors. *Advanced Functional Materials* **2018,***28*, 1804150.

3. Wang, Y.; Ding, J.; Zhao, Z.; Wang, Y., A Cerium Doped Scandate Broad Orange-Red Emission Phosphor and its Energy Transfer-Dependent Concentration and Thermal Quenching Character. *Inorganic Chemistry* **2018,***57* (23), 14542-14553.
4. Lü, W.; Jia, Y.; Zhao, Q.; Lv, W.; You, H., Design of a luminescence pattern via altering the crystal structure and doping ions to create warm white LEDs. *Chemical Communications* **2014,***50*, 2635-2637.
5. Lv, W.; Jia, Y.; Zhao, Q.; Jiao, M.; Shao, B.; Lü, W.; You, H., Crystal Structure and Luminescence Properties of $Ca_8Mg_3Al_2Si_7O_{28}$:Eu^{2+} for WLEDs. *Advanced Optical Materials* **2014,***2*, 183-188.
6. Hecht, C.; Stadler, F.; Schmidt, P. J.; auf der Günne, J. S.; Baumann, V.; Schnick, W., $SrAlSi_4N_7$:Eu^{2+}−A Nitridoalumosilicate Phosphor for Warm White Light (pc)LEDs with Edge-Sharing Tetrahedra. *Chemistry of Materials* **2009,***21*, 1595-1601.
7. Masai, H.; Okada, G.; Torimoto, A.; Usui, T.; Kawaguchi, N.; Yanagida, T., X-ray-induced Scintillation Governed by Energy Transfer Process in Glasses. *Scientific Reports* **2018,***8*, 623.
8. Chen, H.; Patrick, A. L.; Yang, Z.; VanDerveer, D. G.; Anker, J. N., High-Resolution Chemical Imaging through Tissue with an X-ray Scintillator Sensor. *Analytical Chemistry* **2011,***83*, 5045-5049.
9. Bulin, A.-L.; Truillet, C.; Chouikrat, R.; Lux, F.; Frochot, C.; Amans, D.; Ledoux, G.; Tillement, O.; Perriat, P.; Barberi-Heyob, M.; Dujardin, C., X-ray-Induced Singlet Oxygen Activation with Nanoscintillator-Coupled Porphyrins. *The Journal of Physical Chemistry C* **2013,***117*, 21583-21589.
10. Kamkaew, A.; Chen, F.; Zhan, Y.; Majewski, R. L.; Cai, W., Scintillating Nanoparticles as Energy Mediators for Enhanced Photodynamic Therapy. *ACS Nano* **2016,***10*, 3918-3935.

11. Guo, T.; Lin, Y.; Zhang, W.-J.; Hong, J.-S.; Lin, R.-H.; Wu, X.-P.; Li, J.; Lu, C.-H.; Yang, H.-H., High-efficiency X-ray luminescence in Eu^{3+}-activated tungstate nanoprobes for optical imaging through energy transfer sensitization. *Nanoscale* **2018,***10*, 1607-1612.

12. Grabmaier, B.; Rossner, W.; Leppert, J., Ceramic scintillators for X-Ray computed tomography. *physica status solidi (a)* **1992,***130*, K183-K187.

13. Greskovich, C.; Duclos, S., Ceramic scintillators. *Annual review of materials science* **1997,***27*, 69-88.

14. Buşe, G.; Giuliani, A.; De Marcillac, P.; Marnieros, S.; Nones, C.; Novati, V.; Olivieri, E.; Poda, D.; Redon, T.; Sand, J.-B., First scintillating bolometer tests of a CLYMENE R&D on Li2MoO4 scintillators towards a large-scale double-beta decay experiment. *Nuclear Instruments and Methods in Physics Research Section A: Accelerators, Spectrometers, Detectors and Associated Equipment* **2018,***891*, 87-91.

15. Zhu, M.; Qi, H.; Pan, M.; Hou, Q.; Jiang, B.; Jin, Y.; Han, H.; Song, Z.; Zhang, H., Growth and luminescent properties of Yb:YAG and Ca co-doped Yb:YAG ultrafast scintillation crystals. *Journal of Crystal Growth* **2018,***490*, 51-55.

16. Bachmann, V.; Ronda, C.; Oeckler, O.; Schnick, W.; Meijerink, A., Color point tuning for $(Sr,Ca,Ba)Si_2O_2N_2:Eu^{2+}$ for white light LEDs. *Chemistry of Materials* **2008,***21*, 316-325.

17. Lim, M. A.; Park, J. K.; Kim, C. H.; Park, H. D.; Han, M. W., Luminescence characteristics of green light emitting $Ba_2SiO_4:Eu^{2+}$ phosphor. *Journal of materials science letters* **2003,***22*, 1351-1353.

18. Li, J.; Liang, Q.; Cao, Y.; Yan, J.; Zhou, J.; Xu, Y.; Dolgov, L.; Meng, Y.; Shi, J.; Wu, M., Layered Structure Produced Nonconcentration Quenching in a Novel Eu^{3+}-Doped Phosphor. *ACS Applied Materials & Interfaces* **2018,***10*, 41479-41486.

19. Janulevicius, M.; Marmokas, P.; Misevicius, M.; Grigorjevaite, J.; Mikoliunaite, L.; Sakirzanovas, S.; Katelnikovas, A., Luminescence and luminescence quenching of highly efficient $Y_2Mo_4O_{15}:Eu^{3+}$ phosphors and ceramics. *Scientific Reports* **2016,***6*, 26098.

20. Dexter, D.; Schulman, J. H., Theory of concentration quenching in inorganic phosphors. *The Journal of Chemical Physics* **1954,***22* (6), 1063-1070.

21. Takahashi, K.; Oka, H.; Ohnuki, S., Selective Growth of Noble Gases at Metal/Oxide Interface. *ACS applied materials & interfaces* **2016,***8* (6), 3725-3729.

22. Liao, Y. K.; Jiang, D. Y.; Ji, Y. M.; Shi, J. L. In *Combustion synthesis of nanosized $Y_2Hf_2O_7$ and $Lu_2Hf_2O_7$ powders*, Key Engineering Materials, Trans Tech Publ: 2005; pp 643-646.

23. Zhou, B.-Z.; Zhou, G.-H.; An, L.-Q.; Zhang, F.; Zhang, G.-J.; Wang, S.-W., Morphology-controlled synthesis of yttrium hafnate by oxalate co-precipitation method and the growth mechanism. *Journal of Alloys and Compounds* **2009,***481* (1-2), 434-437.

24. Zhang, Z.; Avdeev, M.; de los Reyes, M.; Lumpkin, G. R.; Kennedy, B. J.; Blanchard, P. E.; Liu, S.; Tadich, A.; Cowie, B. C., Probing Long-and Short-Range Disorder in $Y_2Ti_{2-x}Hf_xO_7$ by Diffraction and Spectroscopy Techniques. *The Journal of Physical Chemistry C* **2016,***120*, 26465-26479.

25. Cun, Y.; Yang, Z.; Liao, J.; Qiu, J.; Song, Z.; Yang, Y., Enhancement of upconversion luminescence of three-dimensional ordered macroporous $Bi_2Ti_2O_7$: Er^{3+},Yb^{3+} by co-doping of Li+ ions. *Materials Letters* **2014,***131*, 154-157.

26. Gupta, S. K.; Sudarshan, K.; Yadav, A. K.; Gupta, R.; Bhattacharyya, D.; Jha, S. N.; Kadam, R. M., Deciphering the Role of Charge Compensator in Optical Properties of $SrWO_4:Eu^{3+}$:A (A=Li^+,Na^+,K^+): Spectroscopic Insight Using Photoluminescence, Positron Annihilation, and X-ray Absorption. *Inorganic chemistry* **2018,***57*, 821-832.

27. Sobierajska, P.; Pazik, R.; Zawisza, K.; Renaudin, G.; Nedelec, J.-M.; Wiglusz, R. J., Effect of lithium substitution on the charge compensation, structural and luminescence properties of nanocrystalline $Ca_{10}(PO_4)_6F_2$ activated with Eu^{3+} ions. *CrystEngComm* **2016,***18*, 3447-3455.

28. Du, S.; Wang, D.; Qiang, Q.; Ma, X.; Tang, Z.; Wang, Y., The dual-model up/down-conversion green luminescence of $Gd_6O_5F_8$: Yb^{3+},Ho^{3+},Li^{+} and its application for temperature sensing. *Journal of Materials Chemistry C* **2016,***4* (29), 7148-7155.

29. Gupta, S. K.; Sudarshan, K.; Ghosh, P. S.; Srivastava, A. P.; Bevara, S.; Pujari, P. K.; Kadam, R. M., Role of various defects in the photoluminescence characteristics of nanocrystalline $Nd_2Zr_2O_7$: an investigation through spectroscopic and DFT calculations. *Journal of Materials Chemistry C* **2016,***4*, 4988-5000.

30. Gupta, S. K.; Zuniga, J. P.; Ghosh, P. S.; Abdou, M.; Mao, Y., Correlating Structure and Luminescence Properties of Undoped and Eu^{3+}-Doped $La_2Hf_2O_7$ Nanoparticles Prepared with Different Coprecipitating pH Values through Experimental and Theoretical Studies. *Inorganic Chemistry* **2018,***57*, 11815-11830.

31. Pathak, N.; Ghosh, P. S.; Gupta, S. K.; Mukherjee, S.; Kadam, R. M.; Arya, A., An Insight into the Various Defects-Induced Emission in $MgAl_2O_4$ and Their Tunability with Phase Behavior: Combined Experimental and Theoretical Approach. *The Journal of Physical Chemistry C* **2016,***120* (7), 4016-4031.

32. Gupta, S. K.; Ghosh, P. S.; Yadav, A. K.; Jha, S. N.; Bhattacharyya, D.; Kadam, R. M., Origin of Blue-Green Emission in α-$Zn_2P_2O_7$ and Local Structure of Ln^{3+} Ion in α-$Zn_2P_2O_7$:Ln^{3+} (Ln = Sm, Eu): Time-Resolved Photoluminescence, EXAFS, and DFT Measurements. *Inorganic Chemistry* **2017,***56*, 167-178.

33. Du, T.; Ilegbusi, O. J., Synthesis and morphological characterization on PVP/ZnO nano hybrid films. *Journal of Materials Science* **2004,***39*, 6105-6109.

34. Prakash, J.; Kumar, V.; Erasmus, L. J. B.; Duvenhage, M. M.; Sathiyan, G.; Bellucci, S.; Sun, S.; Swart, H. C., Phosphor Polymer Nanocomposite: ZnO:Tb^{3+} Embedded Polystyrene Nanocomposite Thin Films for Solid-State Lighting Applications. *ACS Applied Nano Materials* **2018,***1*, 977-988.

35. Gupta, S. K.; Abdou, M.; Ghosh, P. S.; Zuniga, J. P.; Mao, Y., Thermally Induced Disorder–Order Phase Transition of $Gd_2Hf_2O_7$:Eu^{3+} Nanoparticles and Its Implication on Photo- and Radioluminescence. *ACS Omega* **2019,***4*, 2779-2791.

36. Gupta, S. K.; Abdou, M.; Zuniga, J. P.; Ghosh, P. S.; Molina, E.; Xu, B.; Chipara, M.; Mao, Y., Roles of oxygen vacancies and pH induced size changes on photo- and radioluminescence of undoped and Eu^{3+}-doped $La_2Zr_2O_7$ nanoparticles. *Journal of Luminescence* **2019,***209*, 302-315.

37. Pokhrel, M.; Brik, M. G.; Mao, Y., Particle Size and Crystal Phase Dependent Photoluminescence of La2Zr2O7:Eu3+ Nanoparticles. *Journal of the American Ceramic Society* **2015,***98* (10), 3192-3201.

38. Pokhrel, M.; Wahid, K.; Mao, Y., Systematic Studies on $RE_2Hf_2O_7$:5%Eu^{3+} (RE = Y, La, Pr, Gd, Er, and Lu) Nanoparticles: Effects of the A-Site RE^{3+} Cation and Calcination on Structure and Photoluminescence. *The Journal of Physical Chemistry C* **2016,***120*, 14828-14839.

39. Eagleman, Y.; Weber, M.; Derenzo, S., Luminescence study of oxygen vacancies in lanthanum hafnium oxide, $La_2Hf_2O_7$. *J. Lumin.* **2013,***137*, 93-97.

40. Bai, X.; Pucci, A.; Freitas, V. T.; Ferreira, R. A.; Pinna, N., One-step synthesis and optical properties of benzoate-and biphenolate-capped ZrO_2 nanoparticles. *Adv. Func. Mater.* **2012,***22*, 4275-4283.

41. Rauwel, E.; Galeckas, A.; Rauwel, P., Photoluminescent cubic and monoclinic HfO_2 nanoparticles: effects of temperature and ambient. *Mater. Res. Exp.* **2014,***1*, 015035.

42. Perevalov, T.; Aliev, V. S.; Gritsenko, V.; Saraev, A.; Kaichev, V.; Ivanova, E.; Zamoryanskaya, M., The origin of 2.7 eV luminescence and 5.2 eV excitation band in hafnium oxide. *Appl. Phys. Lett.* **2014,***104*, 071904.

43. Gupta, S. K.; Sudarshan, K.; Ghosh, P.; Srivastava, A.; Bevara, S.; Pujari, P.; Kadam, R., Role of various defects in the photoluminescence characteristics of nanocrystalline $Nd_2Zr_2O_7$: an investigation through spectroscopic and DFT calculations. *J. Mater. Chem. C* **2016,***4*, 4988-5000.

44. Gupta, S. K.; Ghosh, P. S.; Reghukumar, C.; Pathak, N.; Kadam, R. M., Experimental and theoretical approach to account for green luminescence from $Gd_2Zr_2O_7$ pyrochlore: exploring the site occupancy and origin of host-dopant energy transfer in $Gd_2Zr_2O_7$:Eu^{3+}. *RSC Advances* **2016,***6*, 44908-44920.

45. Gupta, S. K.; Sudarshan, K.; Ghosh, P.; Srivastava, A.; Bevara, S.; Pujari, P.; Kadam, R., Role of various defects in the photoluminescence characteristics of nanocrystalline $Nd_2Zr_2O_7$: an investigation through spectroscopic and DFT calculations. *Journal of Materials Chemistry C* **2016,***4*, 4988-5000.

46. Huignard, A.; Gacoin, T.; Boilot, J.-P., Synthesis and Luminescence Properties of Colloidal YVO_4:Eu Phosphors. *Chemistry of Materials* **2000,***12* (4), 1090-1094.

47. Wei, Z.; Sun, L.; Liao, C.; Yan, C.; Huang, S., Fluorescence intensity and color purity improvement in nanosized YBO_3:Eu. *Applied Physics Letters* **2002,***80* (8), 1447-1449.

48. Wen, S.; Zhou, J.; Zheng, K.; Bednarkiewicz, A.; Liu, X.; Jin, D., Advances in highly doped upconversion nanoparticles. *Nature Communications* **2018,***9* (1), 2415.

49. Blasse, G., Energy transfer in oxidic phosphors. *Phys. Lett. A* **1968,***28*, 444-445.

50. Xu, Y.; Zhang, X.; Dai, S.; Fan, B.; Ma, H.; Adam, J.-l.; Ren, J.; Chen, G., Efficient Near-Infrared Down-Conversion in Pr^{3+}–Yb^{3+} Codoped Glasses and Glass Ceramics Containing LaF_3 Nanocrystals. *The Journal of Physical Chemistry C* **2011,***115* (26), 13056-13062.

51. Pokhrel, M.; Brik, M. G.; Mao, Y., Particle Size and Crystal Phase Dependent Photoluminescence of $La_2Zr_2O_7$: Eu^{3+} Nanoparticles. *Journal of the American Ceramic Society* **2015,***98* (10), 3192-3201.

52. Ahemen, I.; Dejene, F. B.; Kroon, R. E.; Swart, H. C., Effect of europium ion concentration on the structural and photoluminescence properties of novel Li_2BaZrO_4: Eu^{3+} nanocrystals. *Optical Materials* **2017,***74*, 58-66.

53. Hsu, C.-C.; Lin, S.-L.; Chang, C. A., Lanthanide-Doped Core–Shell–Shell Nanocomposite for Dual Photodynamic Therapy and Luminescence Imaging by a Single X-ray Excitation Source. *ACS Applied Materials & Interfaces* **2018,***10*, 7859-7870.

54. Gupta, S. K.; Ghosh, P. S.; Yadav, A. K.; Jha, S. N.; Bhattacharyya, D.; Kadam, R. M., Origin of blue-green emission in α-$Zn_2P_2O_7$ and local structure of Ln^{3+} Ion in α-$Zn_2P_2O_7$:Ln(Ln= Sm, Eu): Time-resolved photoluminescence, EXAFS, and DFT measurements. *Inorg. Chem.* **2016,***56*, 167-178.

55. Gupta, S. K.; Mohapatra, M.; Godbole, S.; Natarajan, V., On the unusual photoluminescence of Eu^{3+} in α-$Zn_2P_2O_7$: a time resolved emission spectrometric and Judd–Ofelt study. *RSC Advances* **2013,***3*, 20046-20053.

56. Mahesh, S. K.; Rao, P. P.; Thomas, M.; Francis, T. L.; Koshy, P., Influence of Cation Substitution and Activator Site Exchange on the Photoluminescence Properties of Eu^{3+}-Doped Quaternary Pyrochlore Oxides. *Inorganic Chemistry* **2013,***52*, 13304-13313.

57. Papan, J.; Jovanović, D. J.; Vuković, K.; Smits, K.; Đorđević, V.; Dramićanin, M., Europium(III)-doped $A_2Hf_2O_7$ (A = Y, Gd, Lu) nanoparticles: Influence of annealing temperature, europium(III) concentration and host cation on the luminescent properties. *Optical Materials* **2016,***61*, 68-76.

58. Prakashbabu, D.; Ramalingam, H. B.; Hari Krishna, R.; Nagabhushana, B. M.; Chandramohan, R.; Shivakumara, C.; Thirumalai, J.; Thomas, T., Charge compensation assisted enhancement of photoluminescence in combustion derived Li^+ co-doped cubic ZrO_2:Eu^{3+} nanophosphors. *Physical Chemistry Chemical Physics* **2016,***18*, 29447-29457.

59. Jain, N.; Paroha, R.; Singh, R. K.; Mishra, S. K.; Chaurasiya, S. K.; Singh, R. A.; Singh, J., Synthesis and Rational design of Europium and Lithium Doped Sodium Zinc Molybdate with Red Emission for Optical Imaging. *Scientific Reports* **2019,***9*, 2472.

60. Kumar, R. G. A.; Hata, S.; Ikeda, K.-i.; Gopchandran, K. G., Organic mediated synthesis of highly luminescent Li^+ ion compensated Gd_2O_3:Eu^{3+} nanophosphors and their Judd–Ofelt analysis. *RSC Advances* **2016,***6*, 67295-67307.

61. Puchalska, M.; Zych, E., The effect of charge compensation by means of Na^+ ions on the luminescence behavior of Sm^{3+}-doped $CaAl_4O_7$ phosphor. *Journal of Luminescence* **2012,***132*, 826-831.

62. Avram, D.; Cojocaru, B.; Tiseanu, I.; Florea, M.; Tiseanu, C., Down-/Up-Conversion Emission Enhancement by Li Addition: Improved Crystallization or Local Structure Distortion? *The Journal of Physical Chemistry C* **2017,***121*, 14274-14284.

63. Stanton, I. N.; Belley, M. D.; Nguyen, G.; Rodrigues, A.; Li, Y.; Kirsch, D. G.; Yoshizumi, T. T.; Therien, M. J., Europium- and lithium-doped yttrium oxide nanocrystals that provide a linear emissive response with X-ray radiation exposure. *Nanoscale* **2014,***6* (10), 5284-5288.

64. Cao, R.; Chen, G.; Yu, X.; Cao, C.; Chen, K.; Liu, P.; Jiang, S., Luminescence properties of $Ca_3Ti_2O_7$:Eu^{3+}, Bi^{3+}, R+ (R^+=Li^+, Na^+, and K^+) red emission phosphor. *Journal of Solid State Chemistry* **2014,***220*, 97-101.

65. Lopez, O. A.; McKittrick, J.; Shea, L. E., Fluorescence properties of polycrystalline Tm^{3+}-activated $Y_3Al_5O_{12}$ and Tm^{3+}-Li^+ co-activated $Y_3Al_5O_{12}$ in the visible and near IR ranges. *Journal of Luminescence* **1997,***71*, 1-11.

66. Singh, B. P.; Parchur, A. K.; Ningthoujam, R. S.; Ramakrishna, P. V.; Singh, S.; Singh, P.; Rai, S. B.; Maalej, R., Enhanced up-conversion and temperature-sensing behaviour of Er^{3+} and Yb^{3+} co-doped $Y_2Ti_2O_7$ by incorporation of Li^+ ions. *Physical Chemistry Chemical Physics* **2014,***16*, 22665-22676.

67. Gupta, S. K.; Sudarshan, K.; Yadav, A. K.; Gupta, R.; Bhattacharyya, D.; Jha, S. N.; Kadam, R. M., Deciphering the role of charge compensator in optical properties of $SrWO_4$: Eu^{3+}: A (A= Li+, Na+, K+): Spectroscopic insight using photoluminescence, positron annihilation, and X-ray absorption. *Inorg. Chem.* **2018,***57*, 821-832.

68. Abrams, B. L.; Holloway, P. H., Role of the Surface in Luminescent Processes. *Chemical Reviews* **2004,***104*, 5783-5802.

69. Bae, J. S.; Yoon, J. H.; Park, S. K.; Kim, J. P.; Jeong, E. D.; Won, M. S.; Jeong, J. H.; Shim, K. S.; Yang, H. K.; Yi, S. S., Li-Doping effect on the cathodoluminescent properties of Y_2O_3:Eu^{3+} phosphors. *Surface Review and Letters* **2007,***14*, 535-538.